Computational Materials Science 246 (2025) 113399

Contents lists available at ScienceDirect

Computational Materials Science

journal homepage: www.elsevier.com/locate/commatsci

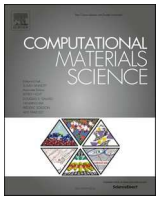

Full Length Article

Atomistic simulation and machine learning predictions of mechanical response in nanotube-polymer composites considering filler morphology and aggregation

Hamid Ghasemi [a], Hessam Yazdani [b,*]

[a] Department of Civil and Environmental Engineering, Howard University, Washington, DC 20059, USA
[b] Department of Civil and Environmental Engineering, University of Missouri, E2509 Lafferre Hall, Columbia, MO 65211, USA

ARTICLE INFO

Keywords:
Polymer composites
Nanotubes
Machine learning
Microscopy
Poisson's ratio
Transverse isotropy

ABSTRACT

Pursuing innovative materials through integrating machine learning (ML) with materials informatics hinges critically upon establishing accurate processing-structure–property-performance relationships and consistently applying them in training datasets. Pivotal to unraveling these relationships is an accurate representation of the microstructure in computational models. In this study, we use transmission electron microscopy (TEM) micrographs of carbon nanotubes (CNTs) within a polymer matrix to construct representative polymer-nanotube composite (PNC) models. We then simulate the models using the coarse-grained molecular dynamics (CG-MD) technique to elucidate the influence of filler morphology and aggregation on the mechanical properties of PNCs. Besides CNTs, we consider cyanoethyl nanotubes (C_3NNT) as a representative of the carbon nitride family, which has remained largely unexplored as a PNC filler for load-bearing purposes. We employ the CG-MD results to train ML models—neural network (NN), support vector regression (SVR), and Gaussian process regression (GPR)—to predict the strain–stress responses of PNCs. Results indicate the profound influence of the filler morphology and aggregation on the elastic and shear stiffness of PNC composites. A high degree of transverse isotropy is observed in the mechanical behavior of composites with perfectly oriented fillers, with Poisson's ratios surpassing conventional upper bounds observed in isotropic materials. For a given morphology, C_3NNT composites exhibit higher stiffness in longitudinal and transverse directions than CNT composites. The ML models demonstrate accuracy in predicting the strain–stress response of the composites, with the GPR model showing the highest accuracy, followed by the NN and SVM models. This accuracy makes the ML models readily integrable into a multiscale modeling framework, significantly enhancing the efficiency of transferring information across scales.

1. Introduction

The ongoing effort to combine machine learning (ML) and materials informatics with the integrated computational materials engineering (ICME) paradigm has accelerated the design of new materials. This effort has led to the emergence of large-scale active learning models that drastically expedite material exploration through an iterative process, thereby reducing the traditional reliance on heuristic methods and minimizing the need for extensive trial and error [1]. At the core of this process are predictive models grounded in processing-structure–property-performance (PSPP) relationships that quickly evaluate the target properties of generated candidates, screen them, and guide the next round of active learning [2,3]. Such models can also be integrated with an inverse design framework to generate potential processing-structure combinations that likely yield specified properties [4].

Developing predictive models for polymer nanocomposites is particularly challenging due to the wide range of compositions, phenomena, and interactions these materials feature. These factors occur across various scales of time, length, complexity, and uncertainty that, in turn, complicate their PSPP relationships [5]. For instance, individual nanotubes (NTs) within a polymer matrix tend to adopt wavy forms and entangle to achieve a more energetically favorable configuration. Aggregation and waviness of NTs affect their intra- and inter-stress transfer, deteriorating the mechanical properties and causing inconsistency in their measured properties [6,7].

Disregarding the influence of filler aggregation and waviness often

* Corresponding author.
E-mail address: hyazdani@missouri.edu (H. Yazdani).

https://doi.org/10.1016/j.commatsci.2024.113399
Received 24 April 2024; Received in revised form 20 August 2024; Accepted 16 September 2024
Available online 17 October 2024

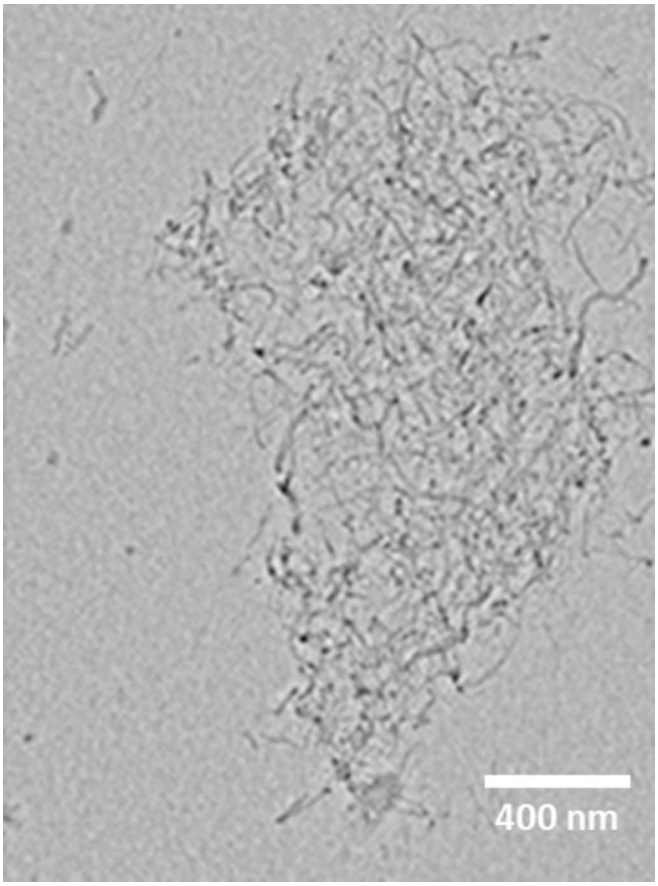

Fig. 1. TEM image of a CNT bundle used to inform microstructure reconstruction [23,26].

leads to overestimating the mechanical properties of polymer composites [8]. This has been consistently corroborated through various studies involving atomistic [9–11], micromechanical [12], and finite element [13] simulations. Most of these studies, however, limited their focus to CNTs, with little to no consideration for the combined influence of filler heterogeneity and morphology on mechanical properties. Predictive ML models were also not in the scope of these works.

The review above emphasizes the need for predictive ML models trained using data that considers filler morphology and the intricate interplays between nanofillers and polymer matrices. However, unraveling these interplays for every conceivable combination of polymers and nanofillers would be impractical. Insights gained from polymer nanocomposites that lend themselves to imaging can provide useful frameworks to develop transfer learning-based approaches to microstructure reconstruction and PSPP predictions, thereby improving the predictive capability and reliability of results. One such polymer is polyvinyl chloride (PVC).

PVC is a widely used thermoplastic polymer [14] known for its high tensile strength, exceptional impact and chemical resistance [15], low moisture absorption, and non-conductive nature [16], making it suitable for various applications ranging from construction materials to healthcare products. Adding materials like carbonaceous or metallic particles to PVC creates pathways for electron flow, enabling its use in applications requiring electrical conductivity. For instance, we have added critical concentrations of carbon black and carbon nanotubes (CNTs) to PVC to impart an engineered degree of conductivity and produce smart composites for strain-sensing applications [17–22]. The micrographs we obtained from CNT-filled PVC across different length scales provided substantial subsurface information that proved very beneficial in reconstructing microstructure for our computational simulations [23].

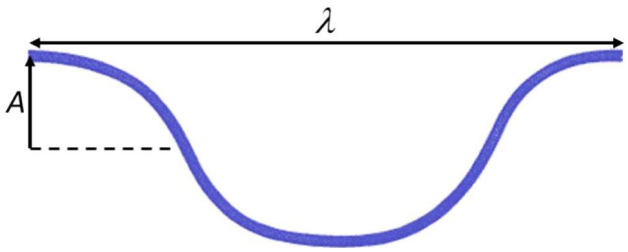

Fig. 2. A schematic of a wavy NT.

Table 1
Summary of simulated NT-PVC models.

Aggregation number, N	Waviness parameter, α (A [nm], λ [nm])
1, 3, 7, 11	0.0 (0.0, 50.0), 0.07 (3.4, 49.2), 0.13 (5.9, 44.4), 0.23 (8.2, 36.0)

This information can be extended to other NTs like cyanoethyl nanotubes (C_3NNTs), which have shown promising mechanical properties in our recent atomistic simulations [24,25]. In a composite form, the presence of nitrogen in carbon nitrides (such as C_3NNTs) may increase their nonbonded interactions with the host polymer and result in high-performance composites, but this topic has remained largely unexplored.

Here, we report the use of transmission electron microscopy (TEM) micrographs to construct PVC composite models filled with CNT and C_3NNT bundles and simulate their tensile response using coarse-grained molecular dynamics (CG-MD). Models differing in the degree of waviness and number of NTs are simulated for tensile stress–strain response. The responses are used to train ML models that accurately predict the strain–stress response of PNCs with unseen waviness and aggregation characteristics.

2. Methodology

2.1. Modeling

Fig. 1 shows the TEM image of a CNT bundle within a PVC matrix that was used to inform the construction of computational models in this study [23,26]. The CNTs in the TEM image were assumed to be ideally represented by a sinusoidal shape as shown in expressed by $y = A\cos(2\pi z/\lambda)$, $z \in [0, \lambda]$, where A and λ are the amplitude and wavelength of the wavy NT, respectively, as shown in Fig. 2 [27]. The waviness parameter is defined as $\alpha = A/\lambda$ to represent the degree of the waviness of the NTs. Also, the degree of filler aggregation was denoted by the aggregation number (N), which is equal to the number of fillers in a model. Four values for α and four values for N were combined, as summarized in Table 1, to define 16 unique models. All CNTs and C_3NNTs were assumed to be armchair (6,6) tubes with an aspect ratio of 62.5 (length to diameter). The length of bundles in all models was 50.0 nm.

Two central MD schemes used for PNCs include all-atom MD (AA-MD) and coarse-grained MD (CG-MD). In AA-MD, each atom in the material system is explicitly represented, and its position and velocity are tracked as they evolve over small time steps. AA-MD allows for a highly accurate representation of the molecular structure and dynamics but is computationally intractable for large systems. In contrast, CG-MD offers enhanced sampling efficiency by lumping neighboring atoms into clusters, termed beads, and employing appropriate functions to represent their interactions accurately. It also allows longer MD simulation times by accommodating larger time steps for configurational sampling. Such balance that CG-MD strikes between computational efficiency and accuracy enables studying larger systems over longer durations that may

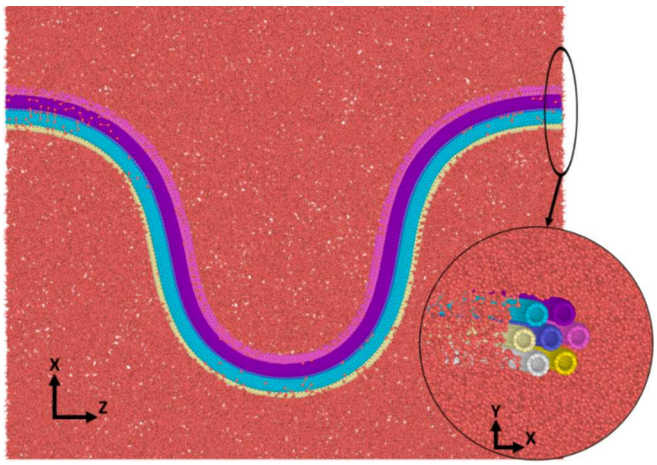

Fig. 3. A sliced view of an MD model filled with seven CNTs. The inset shows its side view.

be inaccessible to AA-MD simulations [28,29]. In this study, AA-MD was used for NTs, while CG-MD was employed to model and simulate the PVC fraction of the models where each C_2H_2Cl monomer of PVC was represented by a bead and interacted with the NTs' AA model.

Modeling involved four stages. First, for a given set of α and N, an AA-MD simulation was performed on straight filler(s) to deform them into the wavy configuration corresponding to the α value. The filler(s) coordinates were recorded at the end of the simulation. Next, a self-avoiding random walk algorithm was used to randomly place 1,000-bead PVC chains around the filler(s). The number of chains in each representative volume element (RVE) was chosen to achieve a filler content of 3 wt% while ensuring a density of approximately 1.3 g/cm^3, consistent with the density of pure PVC. In the third stage, the PVC part of the model was relaxed for 42 ns (ns) to eliminate residual stresses in all dimensions following four steps: the part was 1) amorphized by elevating the temperature to 1000 K under canonical (NVT) ensemble, 2) cooled down to 300 K in 1 ns, 3) allowed to relax over 20 ns under the NVT ensemble, and 4) further relaxed over 20 ns under the isothermal-isobaric ensemble (NPT) ensemble at 300 K with Berendsen thermostat and barostat. The fillers were 'fixed' during this relaxation episode to avoid having them influenced by elevated temperatures. Finally, the entire model (PVC chains and NTs) was relaxed for 1 ns under the NPT ensemble before the simulations, as described in the next section. The coordinates of the model constituents were recorded for later recall in the tensile simulations. Fig. 3 shows the final structure of a model with seven CNTs (N=7) and a waviness parameter of $\alpha = 0.23$.

2.2. Simulations

Interactions among PVC beads were described using a CG force field that we have previously developed and reported elsewhere [30]. The Tersoff potential function [31] defined the interactions among CNT and C_3NNT atoms. The nonbonded interactions were modeled using the van der Waals (vdW) formulation. A time step of 1 fs (fs) was used, and periodic boundary conditions (PBC) were applied in all directions of the model. The simulation box was sized so that the distance between the box edge and the bundle edge was greater than the vdW cutoff, ensuring accurate simulation of the bundles in periodic RVEs without unintended overlaps or interactions. All MD simulations were performed with LAMMPS [32] and visualized with OVITO [33].

The models were assumed to be orthotropic [27] because the filler has different reinforcing effects in longitudinal (chord) and transverse directions—in orthotropic materials, elastic properties are direction-dependent at each point, but there are three mutually orthogonal planes of symmetry with respect to which stretch and shear modes are uncoupled, and also the three shear modes are uncoupled from one another [34]—the orthotropic constitutive law (stiffness matrix) of orthotropic, elastic materials relating the state of stress to the state of strain contains nine coefficients, assuming finite strain. These coefficients can be computed by subjecting a material to uniaxial tension/compression in three principal directions (1, 2, 3) and in-plane shear in the 1–2, 1–3, and 2–3 planes, as shown in Fig. 4. Nine independent elastic constants of the material can then be calculated from the elastic coefficients (e.g., see [27] for the formulation). These constants with reference to the principal material directions 1, 2, and 3 (Fig. 4) include Young's moduli E_1, E_2, E_3, shear moduli G_{12}, G_{13}, G_{23}, and Poisson's ratios ν_{12}, ν_{13}, and ν_{23}, where the subscripts denote the face and direction of stress, respectively. Here, the models were subjected to uniaxial tension and shearing scenarios as described at the rate of 0.001 Å/fs. The simulations involved plugging the previously curved NTs into a new simulation box and relaxing them for 1 ns under NPT at 300 K and zero pressure before applying uniaxial/shear deformations.

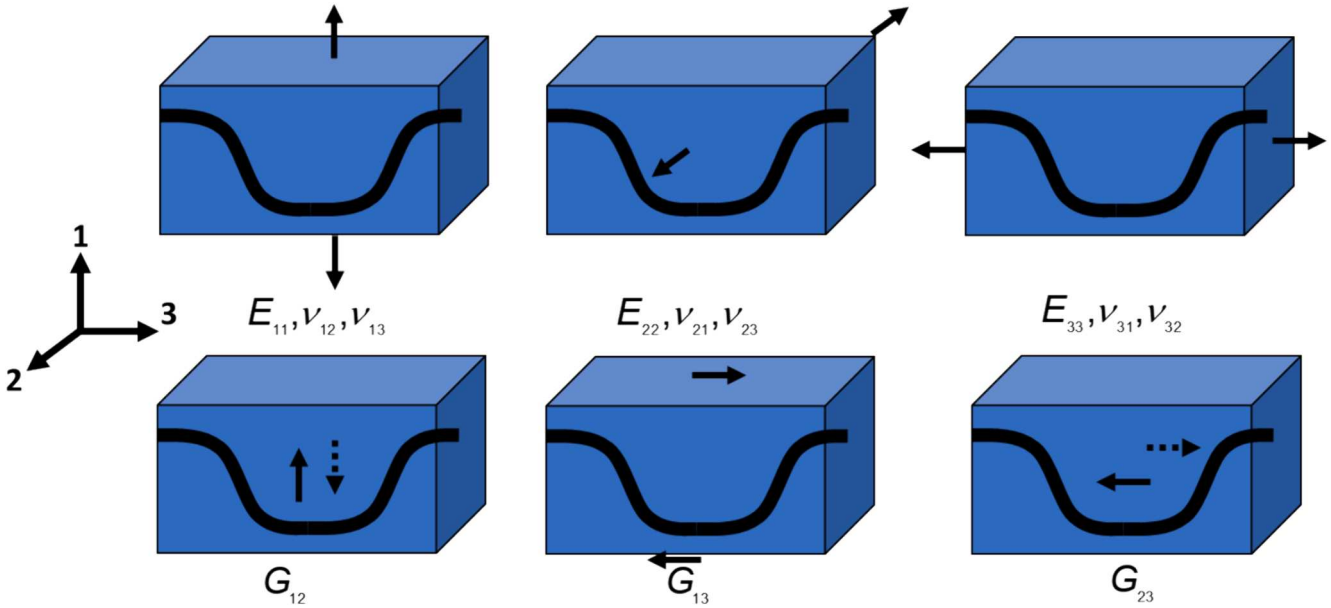

Fig. 4. Schematic of the loading scenarios used to derive elastic constants.

2.3. Machine learning (ML) models

Neural networks (NNs), Gaussian process regression (GPR), and support vector regression (SVR) are examples of ML algorithms that have extensively been used to predict material properties [35–37]. Like any other ML algorithm, they vary significantly in their approaches, strengths, and suitability for different data types and tasks.

2.3.1. Neural networks (NNs)

NNs are ML models inspired by the human brain. They have evolved into a broad family of algorithms and architectures that can tackle a wide range of complex tasks. NNs are composed of nodes and edges, loosely mimicking brain neurons and synapses that connect them. The nodes are arranged in an architecture comprising an input layer, one or more hidden layers, and an output layer. Each node in a layer computes a weighted sum of its inputs. Given n as the total number of inputs x_i being summed for the current node j, the weighted sum of node j is calculated as [38]:

$$z_j = \sum_{i=1}^{n} w_{ij} x_i + b_j \tag{1}$$

where w_{ij} is the weight associated with the connection between nodes i and j, and b is the bias of node j. The weighted average is then passed through an activation function a_j to produce the node's output:

$$a_j = \sigma(z_j) \tag{2}$$

The weights and biases are usually initialized with small random values and then adjusted over many iterations (epochs) until the network's performance meets the desired criteria (e.g., a prescribed mean square error, MSE). The highly flexible architecture of NNs enables them to learn complex patterns but makes their mechanism opaque and their outputs challenging to interpret. Also, the performance of NNs heavily depends on the size of the dataset, with them often yielding poor predictions if the dataset is sparse [39].

2.3.2. Gaussian process regression

Gaussian process regression (GPR) is a nonparametric approach for modeling complex relationships between inputs and outputs without assuming a predefined form for the underlying function or distribution [41]. In other words, GPR's predictions are influenced explicitly by the observations in the dataset. This means that, unlike methods like linear regression, GPR does not require predefined basis functions that match the system's response. This flexibility enables GPR to model highly nonlinear responses using only a few parameters. Another key feature of GPR is that it offers uncertainty estimation for predictions, differentiating between the quality of predictions in interpolation versus extrapolation scenarios.

GPR uses prior knowledge about a system's responses across its covariate (independent variables) domain and uses observed data to update this knowledge. This prior knowledge is represented using a joint multivariate normal probability distribution function (PDF), which assumes that the function values at different points in the input vector are jointly Gaussian distributed.

Let $\mathbf{x} = \{x_1, x_2, \ldots, x_D\}$ be the input vector (D observed locations), $\mathbf{y}$ be the observed target vector, and $f(\mathbf{x})$ be the function value. If the distribution over function value is assumed to be described by a Gaussian process (GP) defined as—in a GP, any finite collection of random variables is jointly Gaussian distributed—:

$$f(\mathbf{x}) \sim \mathcal{GP}(m(\mathbf{x}), k(\mathbf{x}, \mathbf{x}')) \tag{3}$$

where $m(\mathbf{x})$ and $k(\mathbf{x},\mathbf{x}')$ are the mean function and covariance function (kernel) of $f(\mathbf{x})$ at observed locations defined as

$$m(\mathbf{x}) = \mathbb{E}[f(\mathbf{x})] \tag{4}$$

$$k(\mathbf{x}, \mathbf{x}') = \mathbb{E}[(f(\mathbf{x}) - m(\mathbf{x}))(f(\mathbf{x}') - m(\mathbf{x}'))] \tag{5}$$

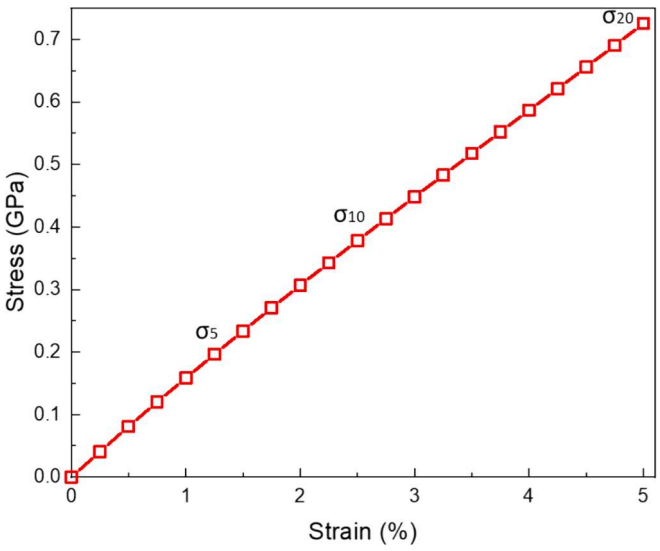

Fig. 5. Illustration of stress–strain data points used for training and testing ML models.

GPR updates this joint prior PDF to obtain the posterior distribution over the function values at any new input vector $\mathbf{x}^* = \{x_{*1}, x_{*2}, \ldots, x_{*P}\}$ (P prediction locations). This posterior distribution at prediction locations, conditioned on D observations, remains Gaussian and is given by:

$$f(\mathbf{x}_*) \sim \mathcal{GP}(m(\mathbf{x}_*), \sigma^2(\mathbf{x}_*)) \tag{6}$$

where the posterior mean vector and covariance matrix at prediction locations are:

$$m(\mathbf{x}_*) = k(\mathbf{x}_*, \mathbf{x}) k(\mathbf{x}, \mathbf{x})^{-1} \mathbf{y} \tag{7}$$

$$\sigma^2(\mathbf{x}_*) = k(\mathbf{x}_*, \mathbf{x}_*) - k(\mathbf{x}_*, \mathbf{x}) k(\mathbf{x}, \mathbf{x})^{-1} k(\mathbf{x}, \mathbf{x}_*) \tag{8}$$

in which $k(\mathbf{x}_*, \mathbf{x})$ is the covariance matrix between the new and training input vectors, and $k(\mathbf{x}, \mathbf{x})^{-1}$ is the inverse of the covariance matrix from the prior distribution [42,43]. GPR has been shown to outperform NNs and SVMs when the training dataset is small, making it a competitive choice because it can achieve high accuracy by learning from fewer simulations, whereas otherwise, extensive and computationally expensive MD simulations would be required to produce sufficient data. However, when dimensionality is large (D>1000, which is unlikely in materials science), building prior knowledge matrices becomes computationally inconvenient [43]. Like NNs, it also suffers from poor interpretability [44].

2.3.3. Support vector regression (SVR)

Support vector machines for regression, also known as support vector regression (SVR), use a different objective function compared with other regression techniques. Instead of minimizing the ordinary least square (OLS), SVR seeks to find a hyperplane that fits most of the data within a specified margin. The hyperplane can then be used to determine the most likely label for unseen data [45]. SVR employs a kernel function to map the input data to a higher-dimensional feature space, making it easier to define the hyperplane. The prediction made by an SVR model is expressed as:

$$y(x) = \sum_{i=1}^{N} w_n K(x, x_n) + b \tag{9}$$

where ω_n represents the weights, b is the bias term, $K(x, x_n)$ is the kernel function, and N is the number of features. SVR uses OLS as a constraint for regression accuracy, making it less prone to overfitting [46]. This technique is beneficial when the relationships between features and the

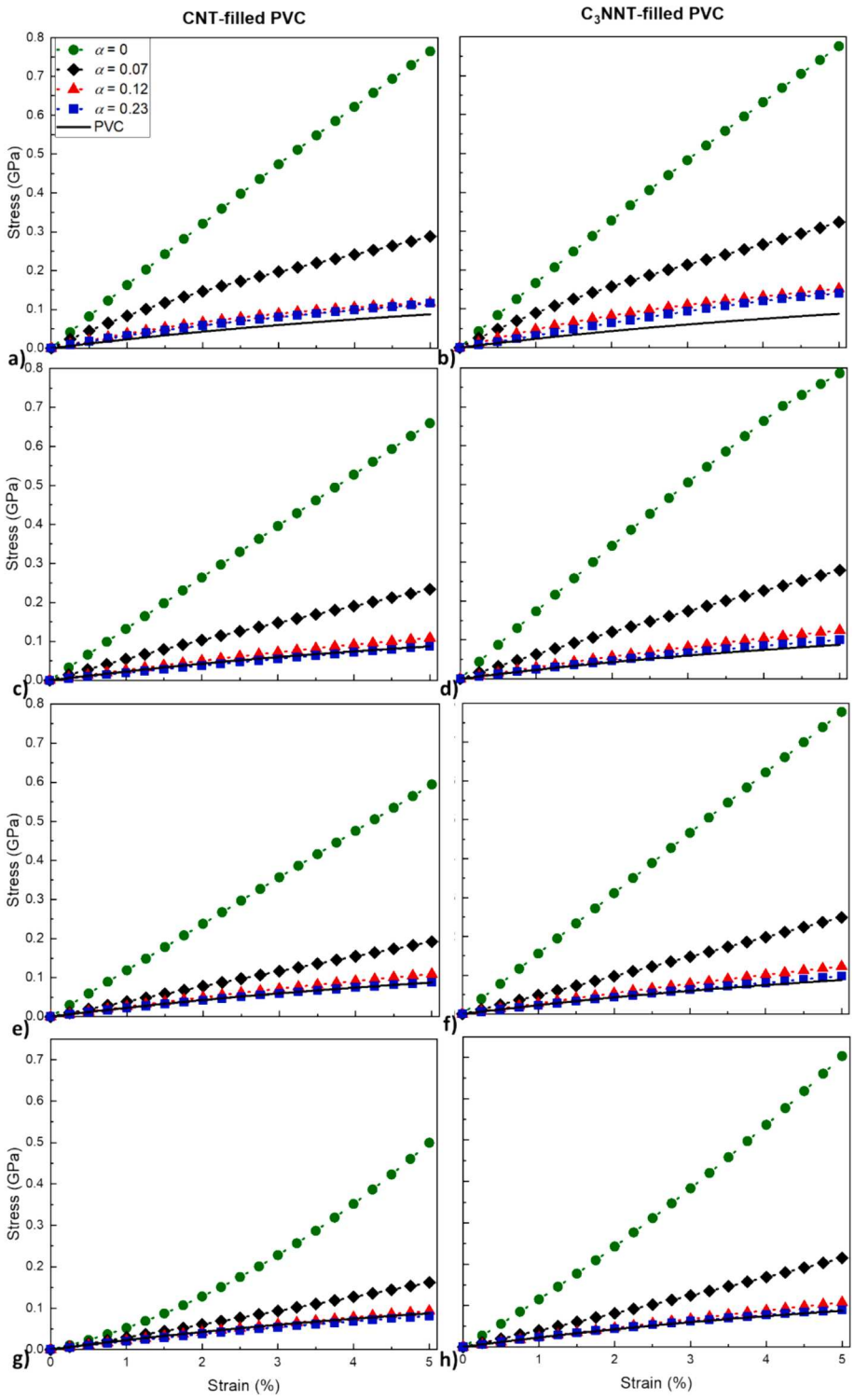

Fig. 6. Influence of filler waviness and aggregation on longitudinal strain–stress response of PVC composites: a and b) N=1, c and d) N=3, e and f) N=7, and g and h) N=11.

target variable are nonlinear. However, similar to GPR, implementing SVR can increase the computational costs of training on large datasets [47].

In this study, for ML training and testing, the first 5 % strain leg of the strain–stress curves was divided into 20 equal segments (i.e., 0.25 % increments), and the stress and strain values at the end of each segment were recorded (σ_i, ε_i, $i = 1$–20) (Fig. 5). To train and test the ML models, the strain values, waviness parameter, and aggregation number were used as the independent variables, and stresses in three directions were used as the dependent variables. A random 80–20 split was used for training and testing the ML models.

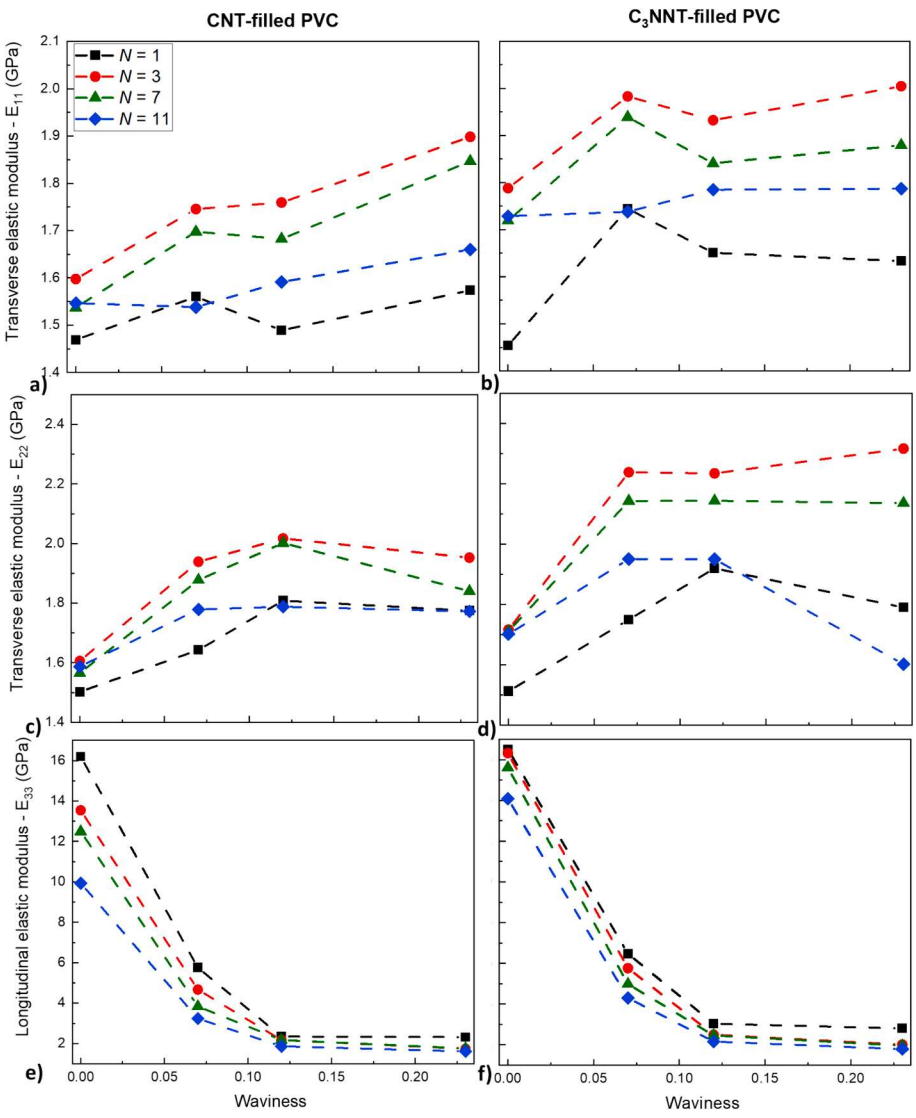

Fig. 7. Influence of waviness and aggregation on tensile elastic moduli of PVC composites in a, b) transverse direction, E_{11}, c, d) transverse direction, E_{22}, and e, f) longitudinal direction, E_{33}. Simulated elastic modulus of PVC: 1.46 ± 0.32 GPa.

3. Results and Discussion

3.1. Stress–strain response

Simulations of pure PVC indicated a tensile elastic modulus of 1.46 ± 0.32 GPa, a shear modulus of 0.56 ± 0.04 GPa, and a Poisson's ratio of 0.28 ± 0.01, assuming isotropic behavior due to amorphous structure. In the composite form, PVC was influenced by bundle size and curvature to varying extents, with the filler playing a significant role. Fig. 6 shows the stress–strain response of the simulated PVC and composite models in the longitudinal direction. Generally, all models exhibit a linear response within the range of strain considered. At a given strain, C_3NNT-filled PVC sustained a higher level of stress than CNT-filled PVC. Also, waviness and aggregation significantly reduced stiffness (slope of the curves).

3.2. Elastic modulus response

Fig. 7 shows the influence of waviness and aggregation on the composites' elastic moduli (stiffness) in different directions. The following observations can be made:

a) Fig. 7a, b, c: For a given waviness and aggregation, C_3NNT composites exhibit higher stiffness in longitudinal and transverse directions than CNT composites. At first glance, this observation contrasts with our previous MD works where, for the same chirality of (6,6), individual CNTs were found to be 17 % stiffer than individual C_3NNTs [24,48]. This difference can be explained by stronger nonbonded interactions between C_3NNT fillers and PVC and among C_3NNT fillers compared with those in the CNT composites. Nonbonded interactions play a crucial role due to the high surface-to-weight ratio of 1D fillers like CNT and C_3NNT, resulting in a large interface with PVC. Consequently, the strength of interactions at the interface between PVC and fillers significantly impacts the elastic moduli of nanotube composites. According to energy terms of the vdW formulation for nitrogen and carbon atoms within a comparable interaction cutoff, the nonbonded energy between PVC and a unit cell of C_3NNT filler (which includes six carbon atoms and two nitrogen atoms) is approximately 17 % stronger than the interaction between PVC and a unit cell of CNT consisting of eight carbon atoms. Likewise, the nonbonded interactions between a pair of nitrogen atoms (between two C_3NNTs) are nearly twice as strong as those between a pair of carbon atoms (between two CNTs). This results in

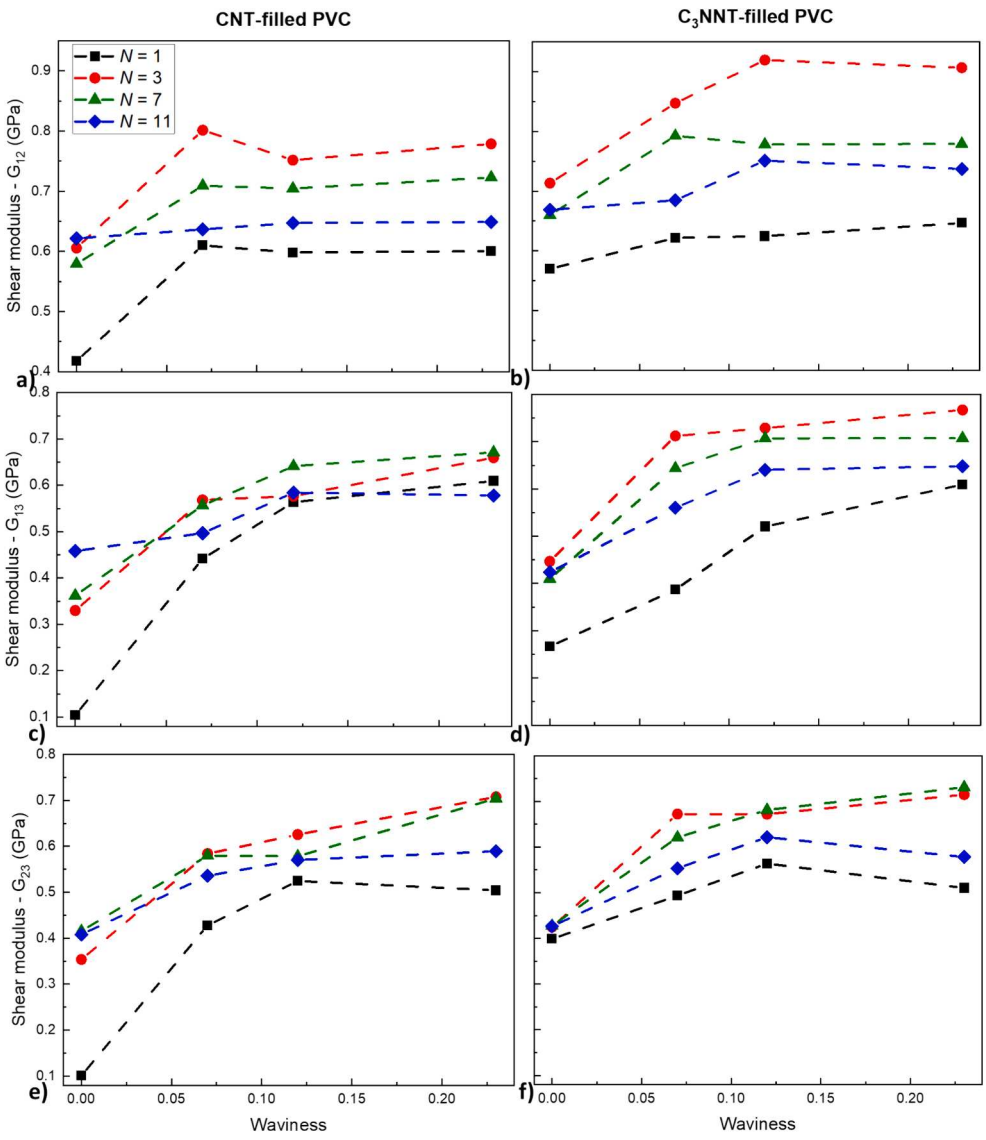

Fig. 8. Influence of waviness and aggregation on shear moduli of PVC composites: a, b) G_{12}, c, d) G_{13}, and e, f) G_{23}. Simulated shear modulus of PVC: 0.56 ± 0.04 GPa.

stronger nonbonded interactions and, consequently, larger elastic moduli for C_3NNT-filled PVC nanocomposites.

b) Fig. 7a and b: Aside from the general enhancement noted in the transverse elastic moduli of the composites compared with pristine PVC, the transverse elastic moduli of the composites consistently increase with the waviness parameter, reaching the maximum improvement of 58 % for C_3NNT where N=3 and $\alpha = 0.23$, and 37 % for CNT where N=3 and $\alpha = 0.12$. This observation, which has previously been made in other composites [27,49], can be attributed to the increased effective interfacial area between the filler and the polymer matrix due to the filler curvature, promoting better load transfer and stress distribution across the composite material. Additionally, waviness may introduce geometric constraints or hinder the movement of polymer chains, thereby reducing the mobility of polymer segments and increasing the overall stiffness of the composite. This influence, however, is indefinite. Beyond a certain level of waviness, the stiffness begins to decrease or level off, possibly due to localized stress concentrations and disorientation or distortion of polymer chains that, in turn, weaken the filler-matrix bonding, compromising load transfer efficiency.

c) Fig. 7a and b: The influence of aggregation on the reinforcing effect of the filler in the transverse direction does not follow a consistent trend. Most composite models become stiffer as the aggregation number increases to N=3 and then soften with further aggregation. This observation can be explained by load transfer and chain mobility changes, as previously noted. C_3NNT composites exhibit higher transverse stiffness than CNT composites and more sensitivity to aggregation and waviness.

d) Fig. 7c Regarding the longitudinal elastic modulus, increased waviness reduces the modulus, irrespective of the aggregation number and filler type. This reduction amounts to nearly 65 % when waviness increases from $\alpha = 0$ to $\alpha = 0.07$ for both CNT and C_3NNT and further decreases to 80 % for $\alpha = 0.12$ and then plateaues. Although waviness and aggregation negatively impact the longitudinal elastic modulus of the composites, the fillers still provide a minimum improvement of 37 % to the stiffness of pristine PVC.

e) While our simulations indicate substantial enhancements in the transverse and longitudinal elastic moduli of CNT- and C_3NNT-filled PVC composites, these values differ significantly from those observed in our experimental studies. Importantly, our simulations, which extended up to 5 % strain, successfully capture the linear

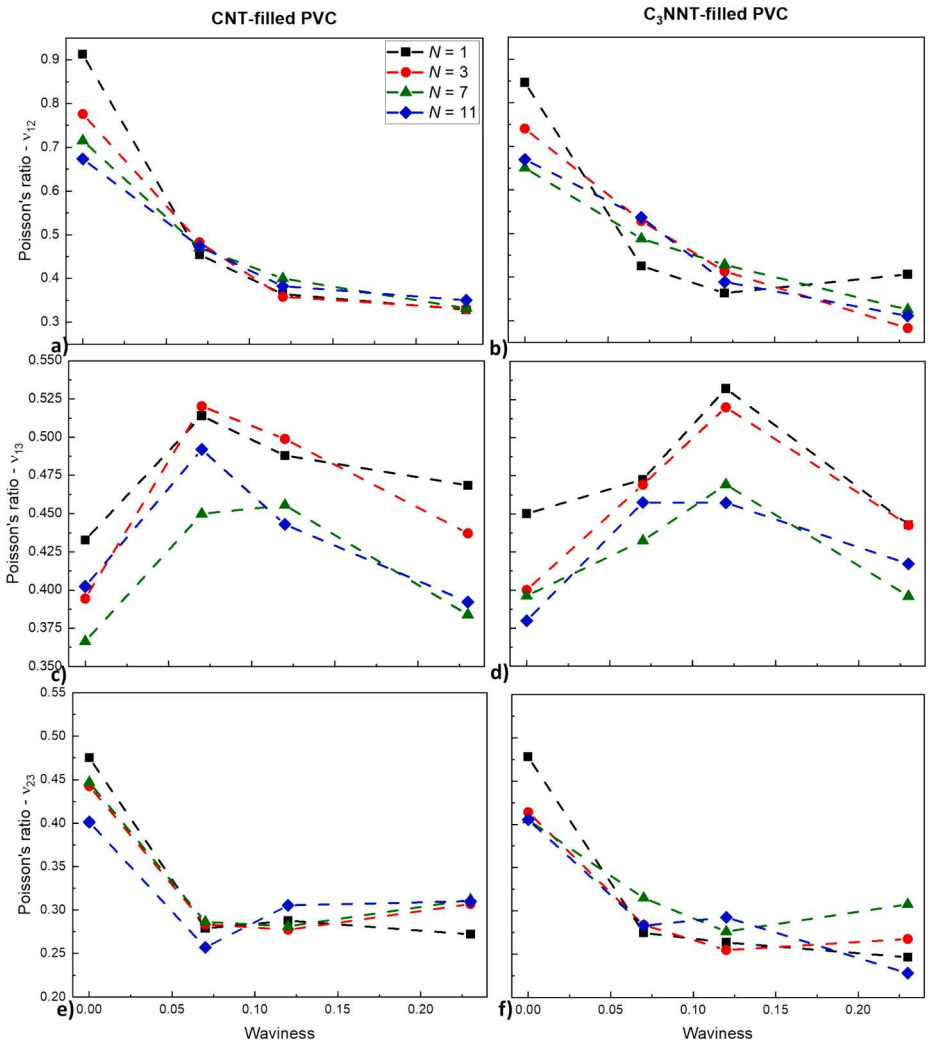

Fig. 9. Influence of waviness and aggregation on Poisson's ratio of PVC composites: a, b) ν_{12}, c, d) ν_{13}, and e, f) ν_{23}. Simulated Poisson's ratio of PVC: 0.28 ± 0.01.

stress–strain response seen in experiments, particularly up to 40 % strain for multi-walled CNT-filled PVC composites. However, the elastic modulus predicted by simulations (~1.8 GPa) is significantly higher than the ~ 9 MPa observed experimentally [20]. This discrepancy can be attributed to several factors: 1) the small length scales and use of PBC in MD simulations, 2) the idealized, defect-free CNTs and perfect interfaces assumed in simulations, which do not account for defects, impurities, or imperfect interfaces present in real materials, 3) the limited time scales in MD compared with the longer time scales in real-time experiments, and 4) differences in CNT orientation, bundle formation, and interaction in real composites, which are not fully captured in the simulations, as we have previously detailed elsewhere [22].

3.3. Shear modulus response

Fig. 8 shows the influence of waviness and aggregation on the shear stiffness of the composites in different planes. The following insights can be drawn:

a) Single, straight NTs reduce the shear modulus of pristine PVC in all planes. This behavior can be attributed to insufficient load transfer due to weak nonbonded interactions in the absence of proper surface functionalization or chemical treatment [50].

b) Similar to transverse elastic moduli, all shear moduli increase with waviness. This observation can be attributed to the filler curvature. Although bonding in our RVEs is primarily governed by vdW interactions, the increased curvature from waviness introduces additional contact points and reduces the mobility of polymer chains, in turn improving shear stiffness [27]. Further improvements can be achieved by functionalizing the filler [11,51].

c) Aggregation increases the shear modulus, with the maximum improvement observed when N=3. This observation could be due to the larger interfacial contact area with the polymer matrix that, in turn, leads to enhanced load transfer and higher shear modulus. In addition, the relatively stronger vdW interactions within nanotube bundles than between the filler and the matrix provide cohesive forces within the bundles that facilitate a more uniform distribution of shear stresses within them, improving shear rigidity. Heavily aggregated fillers may experience non-uniform stress distribution, cause weakened interfacial regions, and facilitate chain mobility, reducing shear stiffness. This observation is consistent with the pattern previously seen and discussed for the elastic moduli.

d) Significant differences are observed between G_{12}, G_{13}, and G_{23} to varying extent depending on aggregation and waviness. Overall, ceteris paribus, shear stiffness in the 2–3 plane (i.e., G_{23}) is the lowest, and that in the 1–2 plane is the highest. Since, in both cases, the filler falls completely in a plane parallel to the shear planes (i.e., the influence of waviness largely eliminated), this observation

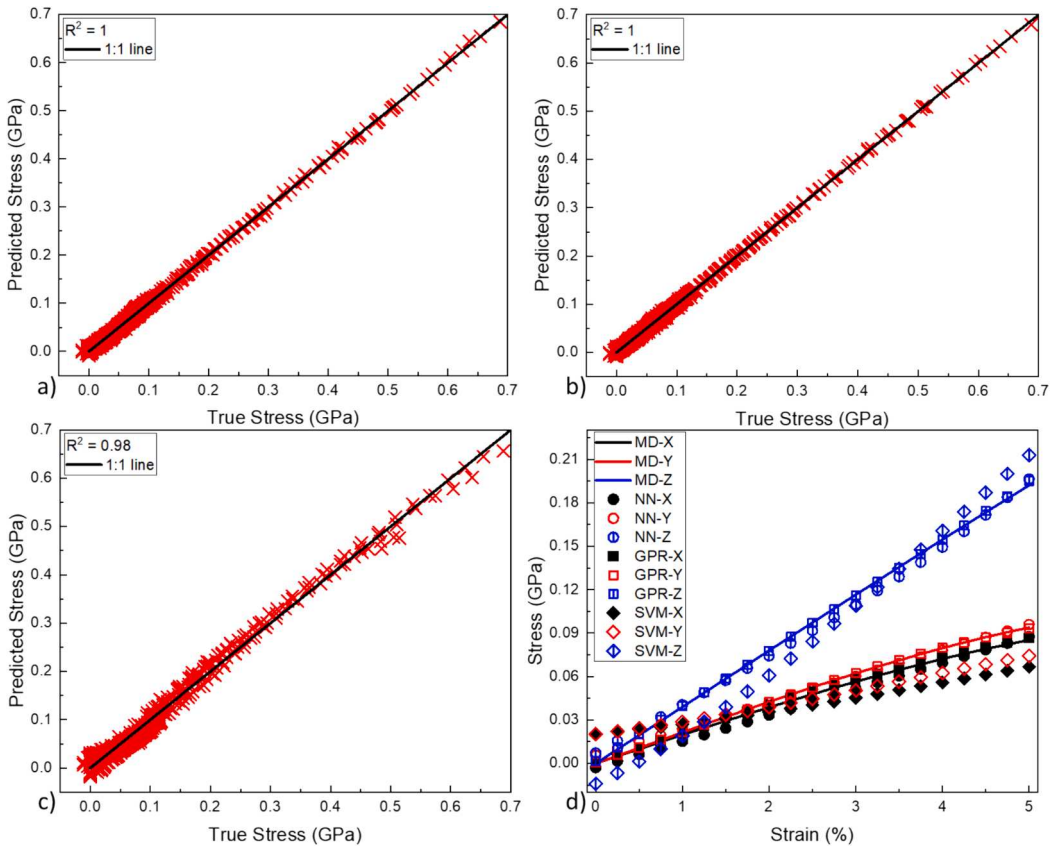

Fig. 10. Performance of a) NN, b) GPR, and c) SVM in predicting stress in all CNT-filled cases. d) Comparison of techniques for stress in three directions (X, Y, Z; respectively, 1, 2, 3) for the 'N=7; α = 0.07′ CNT case.

suggests restricted mobility for polymer chains in the transverse direction, or in other words, the alignment of polymer chains along the longitudinal direction. G_{13} exhibits an intermediate behavior governed perhaps by a competition between tension and compression zones formed in the curve's trough during shear that tend to pull or push the polymer chains away/against the filler(s).

e) Overall, stronger nonbonded interactions between nitrogen atoms in C_3NNT and polymer beads than carbon atoms in CNT and polymer beads manifest themselves in higher shear stiffness for given degrees of waviness and aggregation.

3.4. Poisson's ratio response

Poisson's ratio, ν_{ij}, is the ratio of strain in the *i*-th direction to that in the *j*-th direction when the medium is loaded in the *j*-th direction (based on Maxwell's reciprocal theorem, $\nu_{ij}/\nu_{ji} = E_i/E_j$). For a *D*-dimensional, isotropic medium, ν can be expressed in terms of the isothermal bulk modulus B and the shear modulus G, which represent the size/volumetric and shape/morphological changes of the material, respectively:

$$\nu = (DB/G - 2)/[(D - 1)DB/G + 2] \quad (10)$$

The stability condition for isotropic media requires that $B/G > 0$. This requirement yields the theoretical limits for the Poisson's ratio of these media to be:

$$-1.0 \leq \nu \leq 1/(D - 1) \quad (11)$$

Substituting $D=3$ in Equation (11) gives the theoretical range for Poisson's ratio of a 3D, isotropic material as $-1.0 \leq \nu \leq 0.5$. For 2D solids, this range expands to −1 to 1 [52], and for anisotropic elastic materials, it could be boundless [53,54].

Fig. 9 shows the influence of waviness and aggregation on Poisson's ratio of the composites in different planes. The following observations can be made:

a) Fig. 9a uncovers a notable observation that raises intriguing parallels with the upper bound Equation (2) draws for Poisson's ratio. We observe a Poisson's ratio ν_{12} value close to 1.0 for straight cases. Since ν_{12} is the ratio of strains in transverse directions, this observation suggests a high degree of transverse isotropy in the mechanical behavior of composites with perfectly oriented fillers [55], wherein deformation in one transverse direction induces a nearly equal and opposite deformation in the other transverse direction. This behavior is akin to the mechanical response exhibited by isotropic 2D materials, where Poisson's ratio may exceed the conventional upper bound of 0.5 observed in isotropic 3D materials. It also suggests that certain transversely isotropic materials may behave analogously to 2D materials when loaded in a transverse direction.

b) Poisson's ratio exhibits a distinct trend dependent on the curvature of the nanotube measured in direction 1 upon an extension in direction 3 (i.e., ν_{13}, Fig. 9b). Irrespective of the degree of aggregation and nanotube type, ν_{13} exhibits an initial increase with waviness, followed by a reversal of this trend at higher degrees of curvature, ultimately converging towards values comparable to those observed in straight-bundle cases. This observation suggests complex interactions between the confinement provided by the curved bundle and the alignment of polymer chains. The initial increase could be attributed to the enhanced mobility of the polymer chains facilitated by the presence of a wavy bundle, allowing for greater lateral contraction. However, at higher degrees of waviness, structural constraints imposed by the bundle could hinder this lateral contraction, leading to a decrease in ν_{13}.

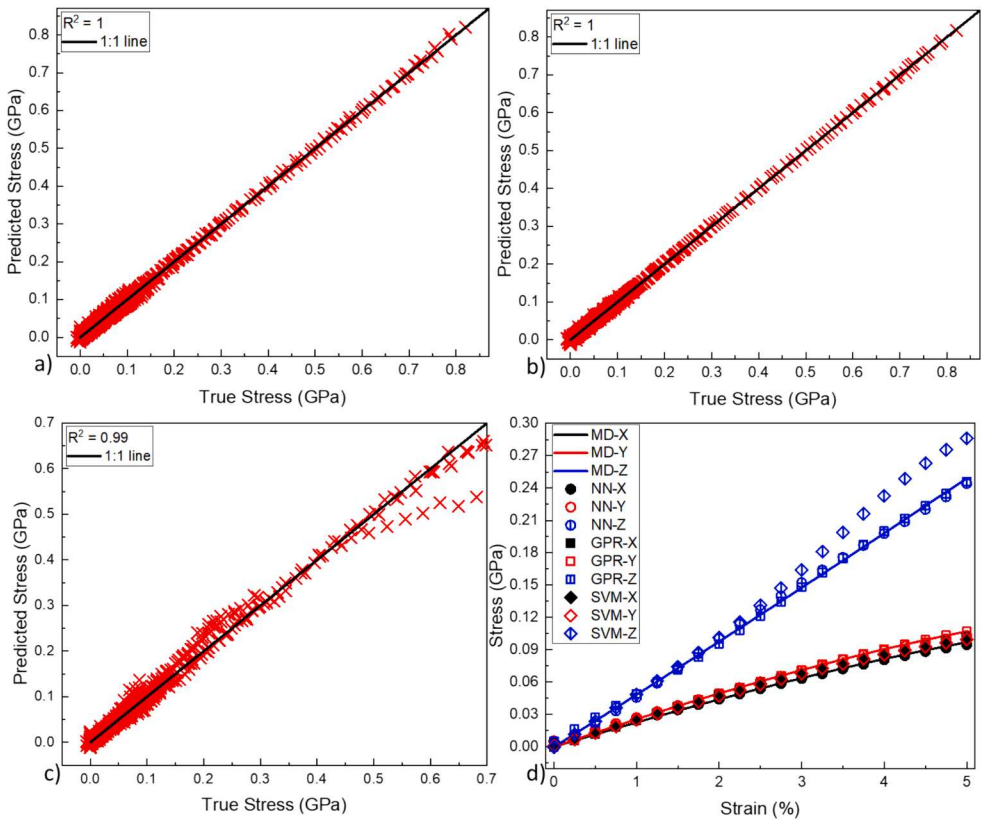

Fig. 11. Performance of a) NN, b) GPR, and c) SVM in predicting stress in all C_3NNT-filled cases. d) Comparison of techniques for stress in three directions (X, Y, Z; respectively, 1, 2, 3) for the 'N=7; α = 0.07′ C_3NNT case.

c) Poisson's ratio calculated in direction 2 when stretched in direction 3 (i.e., ν_{23}, Fig. 9c) shows a consistent decrease as the bundle curvature increases, suggesting heightened confinement experienced by polymer chains at higher bundle curvatures that reduces their lateral movement.
d) In contrast to the differences observed in elastic and shear moduli, there is not a very significant distinction between Poisson's ratios of CNT- and C_3NNT-filled PVC nanocomposites.

3.5. Predictive ML models

Fig. 10 and Fig. 11 show the predictive performance of the ML techniques for CNT and C_3NNT cases, respectively. The models were trained to predict longitudinal and transverse stresses in the composite models given longitudinal strain, waviness parameter, and aggregation number. Performance evaluations are made based on the 1:1 line and the *R-squared* (R^2) metric, representing variance in predictions made for the dependent variables from the independent variables. Consistently high R^2 values for all three models are observed. A closer examination is made in Fig. 10d and Fig. 11d to highlight differences in predictive performance among the three models. The figures correspond to the case where N=7 and $\alpha = 0.07$, and the stress–strain responses in three directions obtained using the MD simulations are also shown as the reference. It can be seen that GPR exhibited superior stress prediction accuracy over SVM and NN. This observation aligns with existing literature suggesting GPR's enhanced accuracy in scenarios involving sparse datasets [40]. Furthermore, NN demonstrated a similar stress prediction accuracy. Its relatively lower computational cost renders it a compelling option for mechanical property predictions, especially in the context of large datasets.

The accuracy observed highlights the efficacy of the ML models in capturing the complex nonlinear behavior of polymer composites. The stress–strain behavior of polymer composites is generally nonlinear and influenced by several factors, including the properties of the polymer and the filler, viscoelastic effects, environmental and loading conditions, the extent of strain, as well as filler morphology and aggregation. Given the extensive range of possible parameter combinations, relying solely on atomistic simulations in a multiscale context would be computationally prohibitive. The ML models developed in this study take some of these parameters as inputs, run them through their learned patterns, and accurately predict the stress–strain response of the composite up to 5 % strain. This level of deformation is below the thresholds commonly stipulated by engineering codes to meet serviceability criteria [21]. The demonstrated accuracy of the ML models renders them suitable for integration into a multiscale framework, enabling an efficient bridging of nanoscale simulations with larger-scale models at a substantially lower computational cost.

4. Conclusion

Coarse-grained molecular dynamics simulations were carried out to understand the influence of filler characteristics, such as bundle size and curvature, on the mechanical properties of PVC composites filled with carbon and cyanoethyl nanotubes (CNTs and C_3NNTs). Overall, C_3NNT composites showed higher stiffness, which was attributed to stronger nonbonded interactions and enhanced load transfer efficiency. Elastic and shear modulus responses indicated the profound role of filler morphology and aggregation in modulating stiffness, with notable differences observed between different planes. Furthermore, analysis of Poisson's ratio response unveiled intriguing parallels with isotropic 2D materials, with upper values close to 1.0. The data was used to develop machine learning models for predicting the mechanical properties of the composite, with Gaussian process regression exhibiting better performance than neural networks and support vector machines. Overall,

these findings contribute to developing predictive models and enhance our ability to design polymer nanocomposites with tailored mechanical properties for various applications. Future research could benefit from incorporating more accurate and representative images obtained from multiple scales of composite materials. Such images will enhance the fidelity of the data used for modeling. They can be integrated into multiscale modeling to advance our understanding of polymer nanocomposites and serve as a platform for producing quality data required to develop accurate and efficient machine learning models for materials discovery.

CRediT authorship contribution statement

Hamid Ghasemi: Writing – original draft, Visualization, Investigation, Formal analysis. **Hessam Yazdani:** Writing – review & editing, Writing – original draft, Supervision, Resources, Project administration, Conceptualization.

Declaration of competing interest

The authors declare that they have no known competing financial interests or personal relationships that could have appeared to influence the work reported in this paper.

Data availability

Data will be made available on request.

Acknowledgments

We gratefully acknowledge the financial support for this research provided by the US National Science Foundation (NSF) under award number 2334166 (formerly 2046332), the US Air Force Office of Scientific Research (AFOSR) under award number FA9550-20-1-0325, and the NVIDIA Hardware Grant Program. We are also grateful to the supercomputing centers at the University of Oklahoma and Arizona State University for granting access to their high-performance computing resources.

References

[1] I. Papadimitriou, I. Gialampoukidis, S. Vrochidis, I. Kompatsiaris, AI methods in materials design, discovery and manufacturing: A review, Comput. Mater. Sci 235 (2024) 112793, https://doi.org/10.1016/j.commatsci.2024.112793.
[2] G.N. Haribabu, J.T. Jegadeesan, C. Bhattacharya, B. Basu, A deep adversarial approach for the generation of synthetic titanium alloy microstructures with limited training data, Comput. Mater. Sci 230 (2023) 112512, https://doi.org/10.1016/j.commatsci.2023.112512.
[3] G.S. Thoppil, J.-F. Nie, A. Alankar, Hierarchical machine learning based structure–property correlations for as–cast complex concentrated alloys, Comput. Mater. Sci 216 (2023) 111855, https://doi.org/10.1016/j.commatsci.2022.111855.
[4] J. Bicerano, D. Rigby, C. Freeman, B. LeBlanc, J. Aubry, Polymer expert – A software tool for *de novo* polymer design, Comput. Mater. Sci 235 (2024) 112810, https://doi.org/10.1016/j.commatsci.2024.112810.
[5] M.A. Akhukov, V.A. Chorkov, A.A. Gavrilov, D.V. Guseva, P.G. Khalatur, A. R. Khokhlov, A.A. Kniznik, P.V. Komarov, M.V. Okun, B.V. Potapkin, V.Y. Rudyak, D.B. Shirabaykin, A.S. Skomorokhov, S.V. Trepalin, MULTICOMP package for multilevel simulation of polymer nanocomposites, Comput. Mater. Sci 216 (2023) 111832, https://doi.org/10.1016/j.commatsci.2022.111832.
[6] J.M. Wernik, S.A. Meguid, Multiscale micromechanical modeling of the constitutive response of carbon nanotube-reinforced structural adhesives, Int. J. Solids Struct. 51 (2014) 2575–2589, https://doi.org/10.1016/j.ijsolstr.2014.03.009.
[7] Y. Wu, C. Wang, T. Yang, Aggregation of nanoparticles and their effect on mechanical properties of carbon nanotube networks, Comput. Mater. Sci 202 (2022) 110970, https://doi.org/10.1016/j.commatsci.2021.110970.
[8] A.R. Alian, S.I. Kundalwal, S.A. Meguid, Multiscale modeling of carbon nanotube epoxy composites, Polymer 70 (2015) 149–160.
[9] A.R. Alian, S.A. Meguid, Molecular dynamics simulations of the effect of waviness and agglomeration of CNTs on interface strength of thermoset nanocomposites, Phys. Chem. Chem. Phys. 19 (2017) 4426–4434, https://doi.org/10.1039/C6CP07464B.
[10] A.R. Alian, S.A. Meguid, Large-scale atomistic simulations of CNT-reinforced thermoplastic polymers, Compos. Struct. 191 (2018) 221–230, https://doi.org/10.1016/j.compstruct.2018.02.056.
[11] A. B.r., D. Ghosh, Influence of nanofiller agglomeration on fracture properties of polymer nanocomposite: Insights from atomistic simulation, Engineering Fracture Mechanics 290 (2023) 109503. DOI: 10.1016/j.engfracmech.2023.109503.
[12] A. Khodadadi, H. Golestanian, F. Aghadavoudi, Two modified multiscale modeling approaches for determination of two-phase and hybrid nanocomposite properties, Proc. Inst. Mech. Eng. C J. Mech. Eng. Sci. 236 (2022) 496–510, https://doi.org/10.1177/09544062211030306.
[13] X. Chen, A.R. Alian, S.A. Meguid, Modeling of CNT-reinforced nanocomposite with complex morphologies using modified embedded finite element technique, Compos. Struct. 227 (2019) 111329, https://doi.org/10.1016/j.compstruct.2019.111329.
[14] L. Vanyorek, E. Sikora, T. Balogh, K. Román, K. Marossy, P. Pekker, T.J. Szabó, B. Viskolcz, B. Fiser, Nanotubes as polymer composite reinforcing additive materials – A comparative study, Arab. J. Chem. 13 (2020) 3775–3782, https://doi.org/10.1016/j.arabjc.2019.01.001.
[15] H. Yazdani, B.E. Smith, K. Hatami, Multi-walled carbon nanotube-filled polyvinyl chloride composites: Influence of processing method on dispersion quality, electrical conductivity and mechanical properties, Compos. A Appl. Sci. Manuf. 82 (2016) 65–77, https://doi.org/10.1016/j.compositesa.2015.12.005.
[16] G. Broza, K. Piszczek, K. Schulte, T. Sterzynski, Nanocomposites of poly(vinyl chloride) with carbon nanotubes (CNT), Compos. Sci. Technol. 67 (2007) 890–894, https://doi.org/10.1016/j.compscitech.2006.01.033.
[17] K. Hatami, A. Hassanikhah, H. Yazdani, B. Grady, Tensoresistive PVC Coating for Sensor-Enabled Geogrids, Journal of Nanomechanics and Micromechanics 4 (2014) A4013016, https://doi.org/10.1061/(ASCE)NM.2153-5477.0000070.
[18] H. Yazdani, K. Hatami, E. Khosravi, K. Harper, B.P. Grady, Strain-sensitive conductivity of carbon black-filled PVC composites subjected to cyclic loading, Carbon 79 (2014) 393–405, https://doi.org/10.1016/j.carbon.2014.07.082.
[19] H. Yazdani, K. Hatami, Sensor-Enabled Geogrids for Stabilization and Instrumentation of Earth Structures, in: Life-Cycle of Engineering Systems:, CRC Press, London, UK, 2016: pp. 1236–1241.
[20] H. Yazdani, B.E. Smith, K. Hatami, Electrical conductivity and mechanical performance of multiwalled CNT-filled polyvinyl chloride composites subjected to tensile load, J. Appl. Polym. Sci. 133 (2016), https://doi.org/10.1002/app.43665.
[21] H. Yazdani, K. Hatami, B.P. Grady, Sensor-Enabled Geogrids for Performance Monitoring of Reinforced Soil Structures, J. Test. Eval. 44 (2016) 20140501, https://doi.org/10.1520/JTE20140501.
[22] H. Yazdani, H. Ghasemi, C. Wallace, K. Hatami, Mechanical properties of carbon nanotube-filled polyethylene composites: A molecular dynamics simulation study, Polym. Compos. 40 (2019) E1850–E1861, https://doi.org/10.1002/pc.25175.
[23] H. Yazdani, B. Smith, K. Hatami, Multiscale 3D dispersion characterization of carbon nanotube-filled polymer composites using microscopic imaging and data mining, in: W.I. Milne, M. Cole, S. Mitura (Eds.), Carbon Nanotechnology, One Central Press, Manchester, UK, 2016.
[24] H. Ghasemi, B. Abraham, J. Rutledge, H. Yazdani, Mechanical properties of C3N nanotubes, Diam. Relat. Mater. 109 (2020) 108090, https://doi.org/10.1016/j.diamond.2020.108090.
[25] H. Ghasemi, J. Rutledge, H. Yazdani, Mechanical properties of defective cyanoethynyl (2D polyaniline – C3N): A comparative molecular dynamics study versus graphene and hexagonal boron nitride, Physica E 121 (2020) 114085, https://doi.org/10.1016/j.physe.2020.114085.
[26] B. Smith, H. Yazdani, K. Hatami, Three-dimensional imaging and quantitative analysis of dispersion and mechanical failure in filled nanocomposites, Compos. A Appl. Sci. Manuf. 79 (2015) 23–29, https://doi.org/10.1016/j.compositesa.2015.08.019.
[27] A.R. Alian, S. El-Borgi, S.A. Meguid, Multiscale modeling of the effect of waviness and agglomeration of CNTs on the elastic properties of nanocomposites, Comput. Mater. Sci 117 (2016) 195–204, https://doi.org/10.1016/j.commatsci.2016.01.029.
[28] R.E. Rudd J.Q. Broughton Coarse-grained molecular dynamics and the atomic limit of finite elements Phys. Rev. B 58 1998 R5893 R896 10.1103/PhysRevB.58.R5893.
[29] A.J. Pak, G.A. Voth, Advances in coarse-grained modeling of macromolecular complexes, Curr Opin Struct Biol 52 (2018) 119–126, https://doi.org/10.1016/j.sbi.2018.11.005.
[30] H. Ghasemi, H. Yazdani, Plastics and sustainability in the same breath: Machine learning-assisted optimization of coarse-grained models for polyvinyl chloride as a common polymer in the built environment, Resour. Conserv. Recycl. 186 (2022) 106510, https://doi.org/10.1016/j.resconrec.2022.106510.
[31] A. Kınacı, J.B. Haskins, C. Sevik, T. Çağın, Thermal conductivity of BN-C nanostructures, Phys. Rev. B 86 (2012) 115410, https://doi.org/10.1103/PhysRevB.86.115410.
[32] S. Plimpton, Fast Parallel Algorithms for Short-Range Molecular Dynamics, J. Comput. Phys. 117 (1995) 1–19, https://doi.org/10.1006/jcph.1995.1039.
[33] A. Stukowski, Visualization and analysis of atomistic simulation data with OVITO–the Open Visualization Tool, Modelling Simul. Mater. Sci. Eng. 18 (2009) 015012, https://doi.org/10.1088/0965-0393/18/1/015012.
[34] K. Bhaskar, T.K. Varadan, Theory of isotropic/orthotropic elasticity, Springer Nature, 2022.
[35] T. Shiraiwa, K. Tamura, M. Enoki, Analysis of kinking and twinning behavior in extruded Mg–Y–Zn alloys by acoustic emission method with supervised machine learning technique, Mater. Sci. Eng. A 768 (2019) 138473, https://doi.org/10.1016/j.msea.2019.138473.

[36] L. Wan, Z. Ullah, D. Yang, B.G. Falzon, Probability embedded failure prediction of unidirectional composites under biaxial loadings combining machine learning and micromechanical modelling, Compos. Struct. 312 (2023) 116837.
[37] B. Ma, N.J. Finan, D. Jany, M.E. Deagen, L.S. Schadler, L.C. Brinson, Machine-Learning-Assisted Understanding of Polymer Nanocomposites Composition-Property Relationship: A Case Study of NanoMine Database, Macromolecules (2023).
[38] S.L. Brunton J.N. Kutz Data-Driven Science and Engineering: Machine Learning, Dynamical Systems, and Control 2019 Cambridge University Press Cambridge 10.1017/9781108380690.
[39] H.P. Lal, A. B.r., D. Ghosh, Prediction of nonlocal elasticity parameters using high-throughput molecular dynamics simulations and machine learning, Eur. J. Mech. A. Solids 103 (2024) 105175, https://doi.org/10.1016/j.euromechsol.2023.105175.
[40] S. Bishnoi, S. Singh, R. Ravinder, M. Bauchy, N.N. Gosvami, H. Kodamana, N.M. A. Krishnan, Predicting Young's modulus of oxide glasses with sparse datasets using machine learning, J. Non Cryst. Solids 524 (2019) 119643.
[41] C.E. Rasmussen, Gaussian Processes in Machine Learning, in: O. Bousquet, U. von Luxburg, G. Rätsch (Eds.), Advanced Lectures on Machine Learning: ML Summer Schools 2003, Canberra, Australia, February 2 - 14, 2003, Tübingen, Germany, August 4 - 16, 2003, Revised Lectures, Springer, Berlin, Heidelberg, 2004: pp. 63–71. DOI: 10.1007/978-3-540-28650-9_4.
[42] C.E. Rasmussen, C.K.I. Williams, Gaussian Processes for Machine Learning, MIT Press, Cambridge, MA, 2006.
[43] J.-A. Goulet, Probabilistic Machine Learning for Civil Engineers, MIT Press, Cambridge, MA, 2020.
[44] D. Burt C.E. Rasmussen M.V.D. Wilk Rates of Convergence for Sparse Variational Gaussian Process Regression International Conference on Machine Learning 2019 PMLR 862 871 accessed January 26, 2021.
[45] D.A. Pisner, D.M. Schnyer, Chapter 6 - Support vector machine, in: A. Mechelli, S. Vieira (Eds.), Machine Learning, Academic Press, 2020, pp. 101–121, https://doi.org/10.1016/B978-0-12-815739-8.00006-7.
[46] R.A. Mozumder, B. Roy, A.I. Laskar, Support Vector Regression Approach to Predict the Strength of FRP Confined Concrete, Arab J Sci Eng 42 (2017) 1129–1146, https://doi.org/10.1007/s13369-016-2340-y.
[47] Z. Yang, X.S. Gu, X.Y. Liang, L.C. Ling, Genetic algorithm-least squares support vector regression based predicting and optimizing model on carbon fiber composite integrated conductivity, Mater. Des. 31 (2010) 1042–1049, https://doi.org/10.1016/j.matdes.2009.09.057.
[48] H. Yazdani, K. Hatami, M. Eftekhari, Mechanical properties of single-walled carbon nanotubes: a comprehensive molecular dynamics study, Mater. Res. Express 4 (2017) 055015, https://doi.org/10.1088/2053-1591/aa7003.
[49] D.-L. Shi, X.-Q. Feng, Y.Y. Huang, K.-C. Hwang, H. Gao, The Effect of Nanotube Waviness and Agglomeration on the Elastic Property of Carbon Nanotube-Reinforced Composites, J. Eng. Mater. Technol 126 (2004) 250–257, https://doi.org/10.1115/1.1751182.
[50] H.-Z. Shan, T.-W. Chou, Transverse elastic moduli of unidirectional fiber composites with fiber/matrix interfacial debonding, Compos. Sci. Technol. 53 (1995) 383–391, https://doi.org/10.1016/0266-3538(95)00026-7.
[51] A. B.r., D. Ghosh, Atomic investigation on optimal interfacial bonding for enhanced fracture properties in polymer nanocomposites, Eng. Fract. Mech. 281 (2023) 109078, https://doi.org/10.1016/j.engfracmech.2023.109078.
[52] K.W. Wojciechowski, Remarks on "Poisson Ratio beyond the Limits of the Elasticity Theory", J. Phys. Soc. Jpn. 72 (2003) 1819–1820, https://doi.org/10.1143/JPSJ.72.1819.
[53] T.C.T. Ting, T. Chen, Poisson's ratio for anisotropic elastic materials can have no bounds, Quart. J. Mech. Appl. Math. 58 (2005) 73–82.
[54] S. Pamulaparthi Venkata, V. Balbi, M. Destrade, G. Zurlo, Designing necks and wrinkles in inflated auxetic membranes, Int. J. Mech. Sci. 268 (2024) 109031, https://doi.org/10.1016/j.ijmecsci.2024.109031.
[55] L. Chen, C. Liu, J. Wang, W. Zhang, C. Hu, S. Fan, Auxetic materials with large negative Poisson's ratios based on highly oriented carbon nanotube structures, Appl. Phys. Lett. 94 (2009) 253111, https://doi.org/10.1063/1.3159467.